Inverse Design of Topographical Templates for Directed Self-Assembly of Block Copolymers

5 AUTHORS, INCLUDING:

Wubin Bai

Massachusetts Institute of Technology

**14** PUBLICATIONS **42** CITATIONS

SEE PROFILE

Optimizing Topographical Templates for Directed Self-Assembly of Block Copolymers via Inverse Design Simulations

Adam F. Hannon,* Yi Ding, Wubin Bai, Caroline A. Ross,* and Alfredo Alexander-Katz*

Department of Materials Science and Engineering, Massachusetts Institute of Technology, Cambridge, Massachusetts 02139, United States

S *Supporting Information*

ABSTRACT: An inverse design algorithm has been developed that predicts the necessary topographical template needed to direct the self-assembly of a diblock copolymer to produce a given complex target structure. The approach is optimized by varying the number of topographical posts, post size, and block copolymer volume fraction to yield a template solution that generates the target structure in a reproducible manner. The inverse algorithm is implemented computationally to predict post arrangements that will template two different target structures and the predicted templates are tested experimentally with a polydimethylsiloxane-*b*-polystyrene block copolymer. Simulated and experimental results show overall very good agreement despite the complexity of the patterns. The templates determined from the model can be used in developing simpler design rules for block copolymer directed self-assembly.
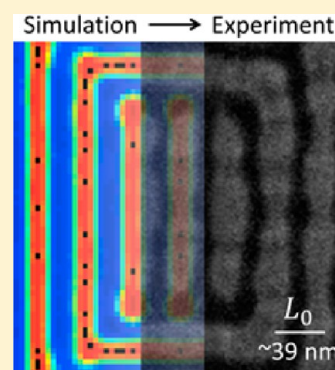
KEYWORDS: PS-b-PDMS, directed self-assembly, block copolymer, inverse design, self-consistent field theory, topographical template

Directed self-assembly of block copolymers (BCPs) continues to be one of the front-running candidates for sub-10 nm lithography.[1−16] Simulation studies of thin films of BCPs are important in predicting the behavior of the film and the geometry of its microdomains under a variety of chemical and topographical boundary conditions.[17−27] Traditionally, simulations are performed by inputting a set of boundary conditions that capture the geometry and surface affinity of the topographical and chemical templates used experimentally to direct the self-assembly of the BCPs, then predicting the resulting microdomain morphology. These "forward" simulation approaches work well for systems where the parameter space of templates can be explored just varying a few key spatial parameters such as the dimensions and spacing of topographical features such as posts.[28−31]

However, for nanolithography it is more likely that the desired or target microdomain morphology will contain complex or nonperiodic features, requiring a correspondingly complicated template. The parameter space required to simulate such structures becomes too large for scans over all possible template features to be practical. An "intuitive" approach is often taken where the template is designed using features that are similar to the target pattern.[32−35] Although this often generates the target structure, it is unlikely to lead to an optimized template with the minimum number of features.

A recent solution to this problem is to use an inverse algorithm that can determine the spatial configuration of template features for a given target pattern.[36,37] In our method,[36] the template consisted of topographical posts which were attractive to one block, and the template was screened through a stochastic minimization process that shares

similarities with a Monte Carlo optimization scheme. This differs in principle from another design approach we have investigated in which post pairs are located on a fixed grid with variable orientation to produce empirical design rules for tile based patterns.[38] Inverse design methods have been applied to other physical systems as well.[39,40] For any inverse method, there is no reason to assume *a priori* that a BCP with a given volume fraction f, degree of polymerization N, and Flory−Huggins interaction parameter χ will be capable of forming the target pattern when directed by a template. Previously, we showed that solutions could be found for different target patterns based on initially guessing the volume fraction and the number of posts. However, to better test the usefulness of such algorithms, a wider range of target and polymer parameters, as well as experimental validation, need to be explored.

Our previous study[36] provided a proof of principle demonstration of the inverse design algorithm, focusing on showing that the algorithm worked computationally for a few target structures. Here, we examine two target patterns, varying both the post number and polymer volume fraction, characterize the solutions through fidelity and connectivity (or topology) criteria, modify the solutions to account for the physical size of the posts, and verify the solutions experimentally with a polystyrene-*b*-polydimethylsiloxane (PS-*b*-PDMS) BCP on an electron beam lithography defined post template.
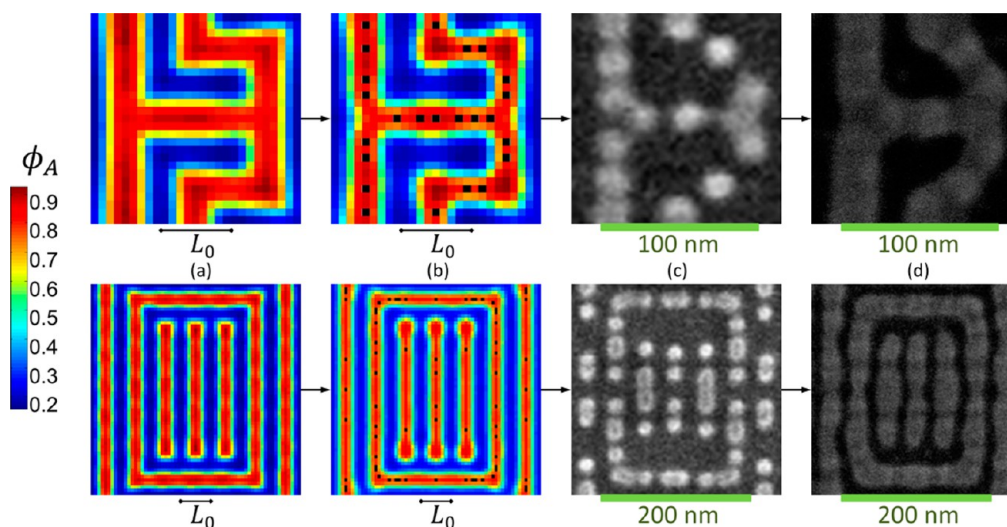
Figure 1. Outline of inverse design process. (a) Two target structures density fields used in testing and optimizing the inverse algorithm. (Top) Structure TS1 which is $3L_0 \times 3L_0$ in size and contains lines, bends, and three way junctions. (Bottom) Structure which is $7L_0 \times 7L_0$ in size with lines, bends, and terminations. (b) Inverse solutions from the inverse design algorithm for the target structures with resulting polymer densities calculated by SCFT. Posts are colored black, minority PDMS regions red, and majority PS regions blue. (c) SEM images of HSQ posts fabricated with electron beam lithography based on the inverse design solutions, accounting for overlap of some neighboring posts. (d) SEM images of oxidized PDMS from BCP self-assembly on post solution templates after reactive ion etching away the PS matrix, demonstrating the inverse design algorithm experimentally.

Theoretical Basis. To model the BCP self-assembly, self-consistent field theory (SCFT) simulations were performed.[41−43] In the simulations, the morphology is defined by a set of density fields ϕ and chemical potential fields Ω on a 2D grid of points with dimensions in terms of L_0, the equilibrium line periodicity of the 2D BCP in an unconstrained system. The density fields are updated and evolved using a pseudospectral method to first solve for the partition function propagators q for the current system chemical potential fields that are integrated over the chain dimension to find the set of ϕ for the current set of Ω. The chemical potential fields which are initiated randomly are solved iteratively using a complex Langevin dynamics scheme that finds the saddle point solution Ω^* for $(\delta H/\delta\Omega)|_{\Omega^*} = 0$ where H is the free energy of the system.[36] This set of Ω^* and their conjugate density fields ϕ^* thus represent an equilibrium morphology of the system, either metastable or minimum energy. For more details on the numerical implementation of SCFT, see previous work by Fredrickson et al.[42,43]

In the inverse design algorithm, a target morphology is constructed by combining simple solutions from forward SCFT simulations for small unit cells that are built up into the desired target pattern.[36] The field solutions for the target structure ϕ_{targ} and Ω_{targ} are used to initiate the system, a fixed number n_{posts} of template posts is added to the system in a random configuration, and through a Monte Carlo like random walk relaxation scheme a configuration of posts that satisfies a stable equilibrium solution to the saddle point condition is found. This process is repeated with several initial conditions of post configurations and a statistically weighted average solution is found, giving a probability density that describes the post positions. A threshold is then applied to the post probability function to produce a template with the desired number of posts. This template configuration is then tested with a forward SCFT simulation to confirm that the solution found does indeed produce the target structure from random initial conditions (see Supporting Information for more details on the inverse algorithm).

To better gauge how well a template solution yields a given target, a root-mean-square average comparison "fidelity" function ξ, representing the difference between the target structure densities and the solution structure densities, is evaluated. We choose the majority component densities ϕ_B since the posts in this study are attractive to the minority block A and occupy minority component volume unless the system becomes oversaturated with posts. The fidelity function is given as $\xi = \int d\vec{r}[(\phi_{B,soln}(\vec{r}) - \phi_{B,targ}(\vec{r}))^2]^{1/2}$. Here $\phi_{B,soln}(\vec{r})$ is the density fields of the SCFT solution for a given post configuration, $\phi_{B,targ}(\vec{r})$ is the target structure density fields, and $\vec{r}$ is the spatial coordinate. The closer ξ is to 0, the better the solution matches the target structure with a value of 0 being a perfect match. For a set of simulations of the same target structure, we renormalize ξ into a fidelity factor $\Xi = \min(\xi)/\xi$, where $\min(\xi)$ is the smallest value of ξ obtained from a set of simulations. A value of $\Xi = 1$ represents the best fidelity factor for that set.

In general a lower value of ξ means a better solution, but a low value does not guarantee that the target pattern has the correct connectivity or topology, that is, that no major defects exist. Thus, in addition to the fidelity function, a binary connectivity criterion is also defined, equal to 1 if all the required interconnections in the minority block are present and no additional interconnections are present, and 0 otherwise.

In a symmetric target structure, the template may not converge to a symmetric solution within a low number of iterations due to asymmetric initial post configurations. To produce a template with the same symmetry as the target pattern, the post probability plot is averaged using the symmetry operation corresponding to the target pattern to save computation time.

Other optimizations of the algorithm may be considered such as incorporating the fidelity function into the algorithm as an additional acceptance criterion, or using a post evolution
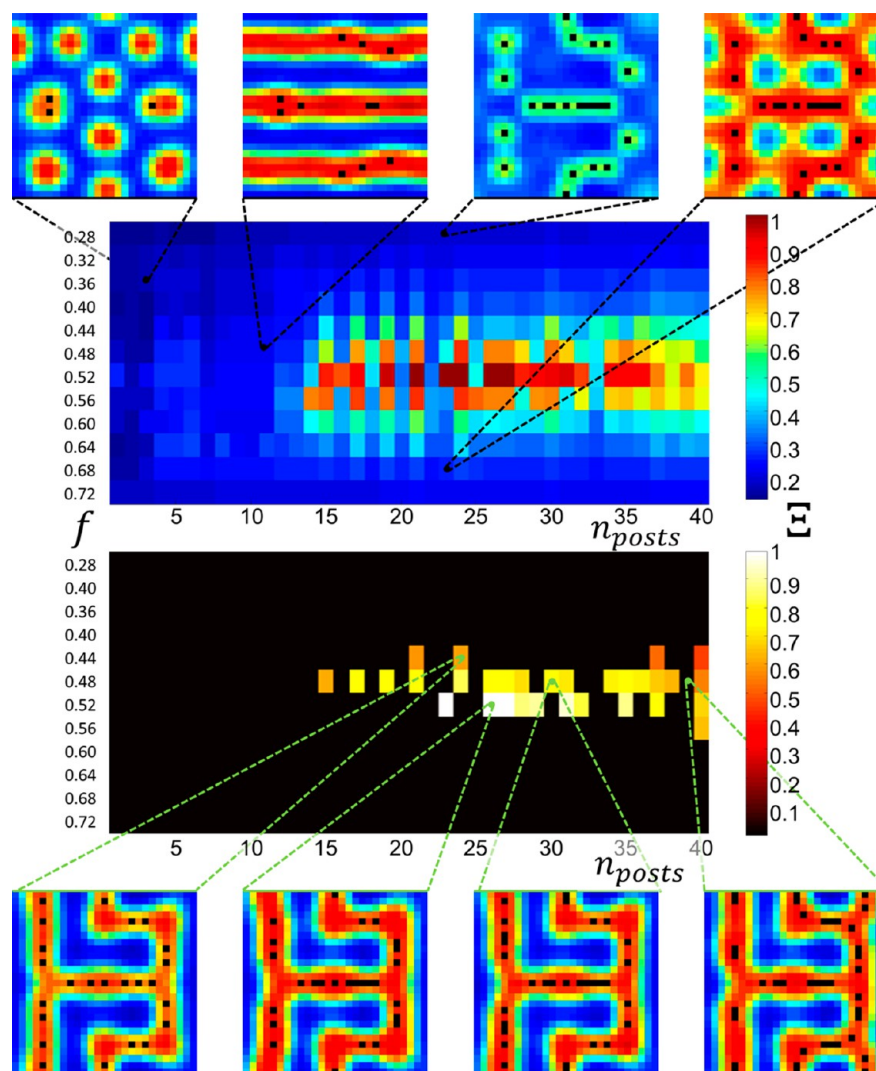
Figure 2. Top phase diagram: Normalized fidelity function Ξ phase diagram for TS1 varying f from 0.28 to 0.72 and n_{posts} from 1 to 40. The highest fidelity function match occurs at $f = 0.52$ and $n_{posts} = 21$. Bottom phase diagram: Binary connectivity phase diagram overlaid on the fidelity function Ξ values where solutions were found. The best solution found in terms of fidelity and connectivity was at $f = 0.52$ and $n_{posts} = 26$. Left to right top insets: Forward SCFT result for $n_{posts} = 3$ and $f = 0.36$, $n_{posts} = 11$ and $f = 0.48$, $n_{posts} = 23$ and $f = 0.28$, and $n_{posts} = 23$ and $f = 0.68$. These are all poor solutions. Left to right bottom insets: Forward SCFT result for $n_{posts} = 24$ and $f = 0.44$, $n_{posts} = 26$ and $f = 0.52$, $n_{posts} = 30$ and $f = 0.48$, and $n_{posts} = 39$ and $f = 0.52$. These are all good solutions.

scheme more advanced than the simple stochastic method used here that allows for the movement of multiple posts to find a more energetically favorable solution. However, even without these optimizations, the algorithm already is relatively fast in computational time. The computation time t (in 2D) goes as $t = aN_XN_Y \ln(N_X)\ln(N_Y)n_{posts}$, where a is a time constant based on the CPU used and length of chain considered, N_X and N_Y are the number of grid points in the X and Y directions, respectively, and n_{posts} is the number of posts used. For our CPU cluster and using an $N_S = 125$ repeat unit coarse graining for the polymer chains, the constant $a = 4.97$ milliseconds per simulation. This means for a single post, a 9×9 grid point L_0 unit cell takes 1.94 s to find an energy minimum configuration. This allows for multiple repeats of the algorithm in the cases examined here for statistical weighting purposes (see Supporting Information for details of the computation time relation).

Experimental Methods. Experimental testing of the simulated templates was done by preparing post templates using electron beam lithography (Elionix) to expose hydrogen silsesquioxane (HSQ), a negative-tone resist. The developed post patterns were then oxidized using an oxygen plasma in an asher, and treated with hydroxyl-terminated PDMS of molecular weight 0.8 kg/mol in a solution of 2 wt % in cyclohexane. After thermally treating the brush for 15 h at 170 °C, the sample was rinsed with toluene to remove excess unreacted brush. A 45.5 kg/mol sample of PS-b-PDMS (PDI $\sim$ 1.15, $f_{PDMS} \sim 0.32$) was then spin coated to a film thickness of 38 nm on the substrate. The sample was solvent annealed for 3 h in either a mixture of 5:1 toluene and heptane vapor or pure toluene. The sample was then treated by reactive ion etching (5 s CF_4 followed by 22 s O_2) to remove the PDMS surface layer, then removing the PS matrix and oxidizing the PDMS microdomains. The samples were imaged in a scanning electron microscope (SEM). Experimental details for similar processes have been described previously[29−31] and further details are given in the Supporting Information.

Results and Discussion. Two simulation target structures were chosen to include bends, junctions, and terminations. These target structures are chosen because these junction, bend, and termination features are difficult to produce controllably without templating. The first target structure was the same one used for an initial demonstration of the inverse algorithm,[36] but the number of posts and the volume fraction of the polymer were not optimized in that work. Figure 1 gives an overview of the inverse design process and its experimental verification. The target density fields of blocks A and B are shown in Figure 1a with red and blue color and are designated henceforth as target structure 1 (TS1) and target structure 2 (TS2). In the simulations of Figure 1, $\chi N = 14$ to reflect the lower effective χ due to solvent incorporation during annealing of the PS-b-PDMS (see Supporting Information for more details on this choice of χN). The Supporting Information shows the free energy versus volume fraction of these structures, which indicate that TS1 had the lowest free energy for $f = 0.55$ and TS2 for $f = 0.45$, where f is the volume fraction of the red block. Figure 1b shows the results of the inverse algorithm where the black squares indicate the calculated post positions with $n_{posts} = 24$ and $n_{posts} = 72$ for TS1 and TS2, respectively. The red and blue show the density of blocks A and B templated by the post positions calculated by SCFT from which it is clear that the template does indeed generate density fields close to those of the target structure. Figure 1c shows experimental post templates fabricated using electron beam lithography. The templates are based on the solutions in Figure 1b except that closely spaced posts were removed or moved as described later in this article to account for proximity effects and the resolution limit of the electron beam. Figure 1d shows the final BCP pattern produced by self-assembly of 45 kg/mol PS-b-PDMS over the templates in Figure 1c. The self-assembly produced patterns close to the target, providing an experimental confirmation of the inverse design model.

We now discuss the effect of post number and volume fraction on the template predicted by the inverse solution, and on the fidelity of the BCP pattern resulting from that template. n_{posts} was varied from 1 to 40 in steps of 1, and f from 0.28 to 0.72 in steps of 0.04. For TS2, since the system has 4-fold symmetry, calculations were only done on a quarter unit cell and the resulting solutions mirrored to form a 4-fold symmetric solution, meaning the actual n_{posts} for the complete pattern varied from 4 to 160 in steps of 4. After finding the template solution for each n_{posts} and f, several SCFT simulations were performed on the template, the resulting density fields averaged, and a fidelity phase diagram and connectivity phase diagram were produced. The phase diagrams for TS1 are shown in Figure 2 with specific solutions highlighted in the insets (for the phase diagrams for TS2, see Supporting Information).

Figure 2 shows both the fidelity function whose value increases toward 1 as the match between the templated structure and the target structure improves and the same data but masked in black where the connectivity is incorrect. Thus the brightest regions indicate the best inverse design solutions, where the template produces a structure that matches well to the target structure and additionally has no missing or extra connections between the microdomains. The insets at top and bottom represent eight solutions for different f and n_{posts}.

The upper phase diagram in Figure 2 shows a range of f, 0.44−0.60 for TS1, where high fidelity solutions are produced above a critical n_{posts}. If f is too low or too high, solutions with missing or extra connections, respectively, between the red

block A are produced, and these solutions are rejected according to the connectivity criterion in the lower phase diagram in Figure 2. Examples are seen in the two top right insets where f is too small in one and too large in the other. However, even for the optimum f, if n_{posts} is too large, the system becomes oversaturated with posts leading to defects such as those seen in the bottom right inset.

The best solution occurred around $n_{posts} = 26$ and $f = 0.52$ for TS1 and around $n_{posts} = 72$ and $f = 0.44$ for TS2. Because each post occupies a single grid point in the simulation and for TS1 there are $N_X \times N_Y = 27 \times 27 = 729$ grid points in the simulation, the posts occupy a volume fraction of $(26/729) \cong 0.036$. Because the posts reside within block A, the total volume fraction occupied by A is $0.52 + 0.036 \cong 0.56$, which is close to the lowest energy volume fraction of 0.55 for structure TS1 shown in Supporting Information Figure S4. For TS2, with $N_X \times N_Y = 63 \times 63 = 3969$ grid points, $f_{posts} = (72/3969) \cong 0.02$, and the total volume fraction occupied by A is $0.44 + 0.02 \cong 0.46$, which is close to the lowest energy volume fraction of 0.45 for structure TS2 shown in Supporting Information Figure S5.

In the simulations of Figures 1 and 2, the posts with their brush layers had a diameter corresponding to ~4.3 nm (1 pixel) for a polymer with $L_0 = 39$ nm (9 pixels), close to L_0 of the PS-b-PDMS used experimentally. Four nanometers is considerably smaller than the minimum diameter of posts that can be produced by e-beam lithography, so it is necessary to understand the effect of post diameter on the self-assembled pattern. Forward SCFT simulations were performed for templates with posts of diameter ~4 nm to ~20 nm and volume fractions of 0.44 to 0.52. To account for overlap between larger diameter posts, posts that were closer than ~L_0/3 (~12 nm) were either eliminated or moved apart as shown in Figure 3. If the posts were effectively a double post motif (two posts only 4 nm apart) one was removed and the other moved to the middle position of the previous two posts. In other cases where multiple posts were near each other, one or more were removed and any remaining post moved between the two
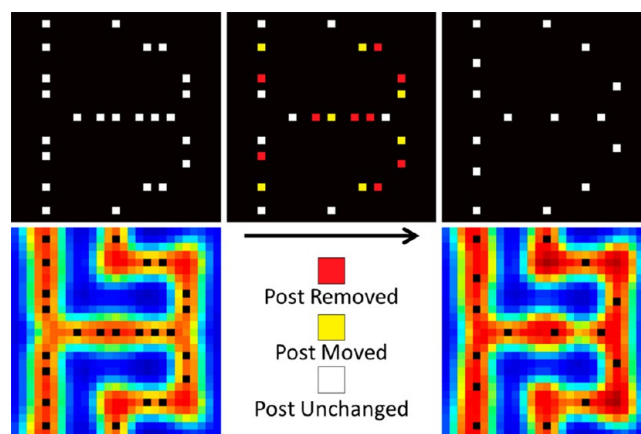

Figure 3. Process for modifying post number and positions to account for overlapping posts of larger size. Left top: Post configuration solution found for TS1 in previous study with 24 posts. Middle top: Posts that are within L_0/3 of their neighbor colored red will be removed, and posts that are colored yellow will be shifted. Right top: Post configuration after removing and moving posts. Left bottom: Polymer density map for the template above. Right bottom: Polymer density map for the template above, showing that the connections are all still present with this modified template.
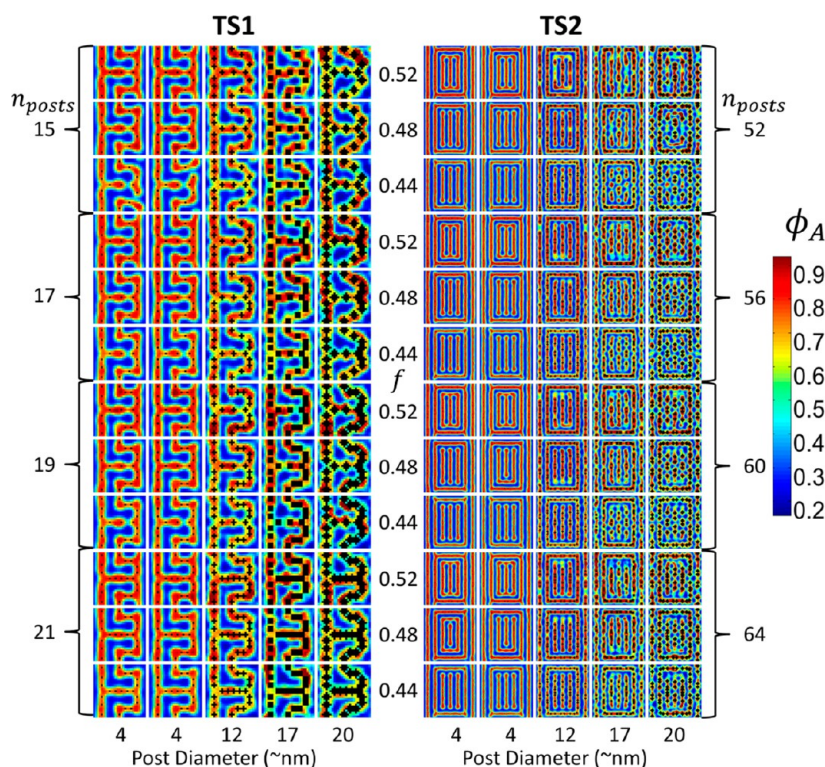
Figure 4. Left: Simulation results for TS1 (left) and TS2 (right) for modified templates in which the post size and volume fraction were varied. The templates were based on the previous study solution for TS1, $n_{posts} = 24$, and the optimum template determined for TS2, $n_{posts} = 72$, with the number of posts reduced by removing posts closer than $L_0/3$ to their neighbors, and shifting other posts to avoid overlap. There are two solutions shown for each of the 4 nm post diameter cases to illustrate the variability obtained from different simulations on the same template.
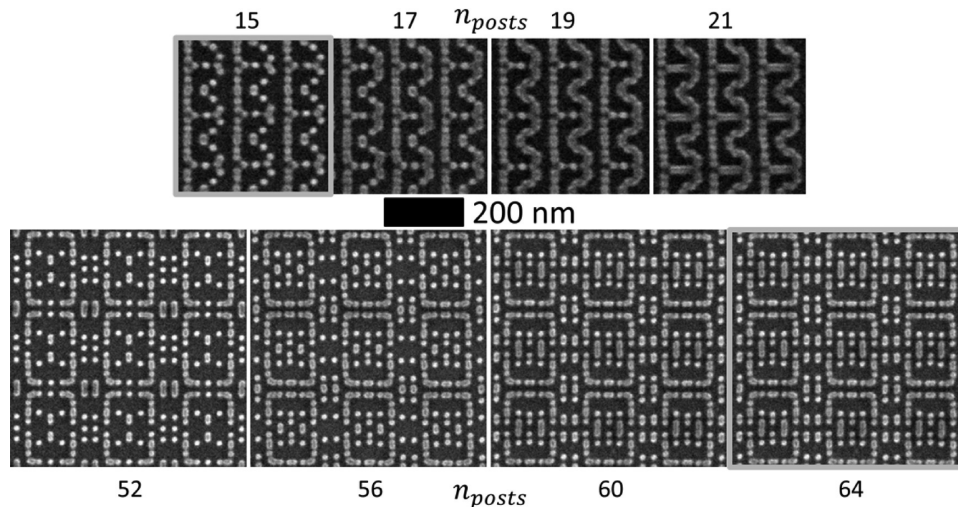

Figure 5. Posts patterns fabricated for experimental validation of inverse algorithm. Patterns that gave best results experimentally are highlighted. Top: Patterns for TS1. Bottom: Patterns for TS2. The micrographs correspond to pattern spacing of $L = 39$ nm.

nearest posts such that the final configuration had no posts closer than $\sim L_0/3$. The solution for TS1 from the previous study, given in Figure 3, had 24 posts. This solution is not the optimum in terms of fidelity found in Figure 2 where $n_{posts} = 26$, but for experimental validation the solution from the previous study was chosen. This solution was reduced to 15 posts, and the best solution for TS2 was reduced from 72 to 52 posts by eliminating posts closer than $\sim L_0/3$. For comparison, three additional templates were considered in which some of the double post features with spacing less than $L_0/3$ were preserved. This corresponds to templates for TS1 with $n_{posts} =$

17, 19, and 21, and for TS2 with $n_{posts} = 56$, 60, and 64. It will be appreciated that these templates, derived by reducing the posts in optimum templates for each target structure, are not identical to the ones determined by the inverse algorithm for the same number of posts.

Results are shown in Figure 4 for TS1 and TS2. Most of the modified templates gave patterns with the correct connectivity for TS1 but increasing post size increased the line edge roughness and caused rounding of the bends in the pattern. For TS2, breaks in the lines often resulted from the templates with the largest posts, and the connectivity was incorrect. As the
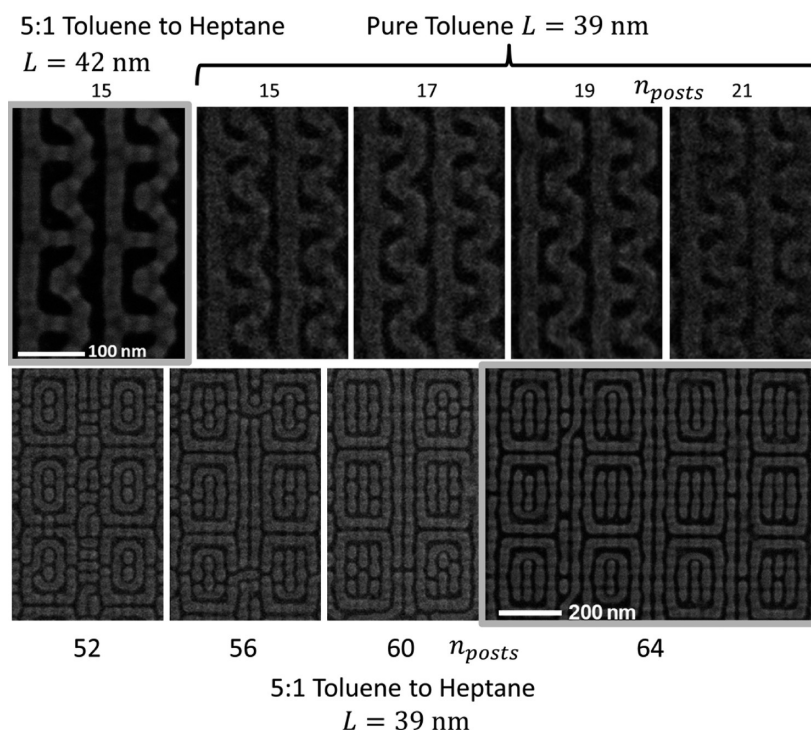
Figure 6. Top: Experimental results for TS1. Patterns with correct connectivity occurred for all four templates and using both 5:1 toluene/heptane and pure heptane vapors. Bottom: Experimental results for TS2. Patterns with best connectivity occurred for the template with 64 posts annealed in 5:1 toluene/heptane, though not all cells produced correct connectivity. Samples with fewest defects are highlighted.

volume of the posts increased, block A surrounded the posts to form a corona rather than making smooth features that connected the posts.

Finally, the inverse design solutions were verified experimentally using templates consisting of posts prepared by electron beam lithography and coated with a layer of PS-b-PDMS of 45 kg/mol, which was solvent annealed and etched to reveal the structure of the minority PDMS microdomains.[29−31] The minimum post diameter was around 14 nm. Four different post patterns were made, each with 10 different values of L, the pattern period length, ranging from 34 to 43 nm in steps of 1 nm as shown in Figure 5.

Figure 6 shows results of self-assembly on the templates for TS1 and TS2. The PDMS microdomains formed the target pattern over a wide range of periods with the best result, i.e. fewest defects, occurring in templates with $L = 39$ nm for samples annealed in vapor from pure toluene, and $L = 42$ nm for samples annealed in vapor from the 5:1 toluene:heptane volume mixture for TS1. The most frequent defect was an additional, separate PDMS circular microdomain appearing in the widest region of PS near the bends in the pattern for larger L. For TS2, the fewest defects occurred at $L = 39$ nm under a solvent annealing condition of 5:1 toluene to heptane compared to pure toluene vapor. The 5:1 vapor annealed samples correspond to a greater volume fraction of PDMS, since heptane is selective to PDMS. The ring-shaped microdomain was the least defective part of the pattern, while the three line segments inside the rings connected in some cases to form a sharp bend. The lines between the rings also showed breaks. These defects are likely due to the reduction in the closely spaced posts which were present in the line segments and in the lines between the rings. Defects in those positions were also more likely for large diameter posts as shown in Figure 4.

These results illustrate some of the features of the template design. Previous work[36] had shown that three way junctions were best stabilized by having posts along the three intersecting lines but no posts at the center of the junction. This observation has now been confirmed experimentally in TS1. The 90° bends were produced reliably by placing dense posts around the bend as seen in the rings of TS2. Terminations on the other hand were more difficult to form as evidenced by the frequent occurrence of defects in TS2, including sharply bent lines from the joining of two line segments. From the simulations, terminations become easier to stabilize for lower volume fraction, but this can lead to more defects in straight lines. This indicates that the most successful templating will be achieved by ensuring the target features are all consistent with the same volume fraction of the polymer.

These results showed that the templates designed from the inverse algorithm were effective in yielding the target pattern, even though the simulations were 2D and the physical system is 3D, and the model does not treat the solvent anneal and subsequent drying process explicitly. Prior work has shown agreement between the lowest energy structures predicted by SCFT and those observed upon solvent annealing PS-b-PDMS, which we attribute to the fact that χN is high even in the swelled film, which undergoes microphase separation while swelled.[44] Some 3D simulations were carried out by mapping the 2D post positions of template solutions into posts in a 3D simulation cell and running a forward SCFT simulation. With appropriate choice of volume fraction, 3D microdomain structures were produced that in plane view resembled the 2D patterns. Future work will correlate 2D and 3D structures in more detail, will consider majority block preferential features, and will optimize the algorithm to derive more general design principles for templates for directed self-assembly.

Conclusions. An inverse design process for determining a template to produce a given target structure from a BCP has been demonstrated in 2D in which both the number of posts and volume fraction of the polymer are varied to optimize the template solution. The quality of the solutions is evaluated through a fidelity function and further screened using a connectivity criterion to ensure the desired topology is present in the solution. The templates were modified by removal of closely spaced posts below the resolution of the lithography system used to make the posts to enable experimental testing. The method was demonstrated for two patterns of PS-*b*-PDMS containing lines, junctions, and terminations, and results showed that the optimum BCP volume fraction is related to the types of features present in the target pattern. These results reveal guidelines for directed self-assembly of BCPs for nanolithography applications, in which nontrivial target patterns are required for which an intuitive design process may not yield the best results.

■ ASSOCIATED CONTENT

Ⓢ Supporting Information

Additional figures, calculation information, simulation information, and SEM micrographs. This material is available free of charge via the Internet at http://pubs.acs.org.

■ AUTHOR INFORMATION

Corresponding Authors

*(A.F.H.) E-mail: thefloyd@mit.edu.
*(C.A.R.) E-mail: caross@mit.edu.
*(A.A.-K.) E-mail: aalexand@mit.edu.

Author Contributions

The manuscript was written through contributions of all authors. All authors have given approval to the final version of the manuscript.

Notes

The authors declare no competing financial interest.

■ ABBREVIATIONS

BCP block copolymer; PS-*b*-PDMS polystyrene-*b*-polydimethylsiloxane; SCFT self-consistent field theory; HSQ hydrogen silsesquioxane; TS1 target structure 1; TS2 target structure 2

■ REFERENCES

(1) Luo, M.; Epps, T. H., III *Macromolecules* **2013**, *46*, 7567−7579.
(2) Koo, K.; Ahn, H.; Kim, S.-W.; Ryu, D. Y.; Russell, T. P. *Soft Matter* **2013**, *9*, 9059−9071.
(3) Hardy, C. G.; Tang, C. *J. Polym. Sci., Part B: Polym. Phys.* **2013**, *51*, 2−15.
(4) Doerk, G. S.; Liu, C.-C.; Cheng, J. Y.; Rettner, C. T.; Pitera, J. W.; Krupp, L. E.; Topuria, T.; Arellano, N.; Sanders, D. P. *ACS Nano* **2013**, *7*, 276−285.
(5) Seino, Y.; Yonemitsu, H.; Sato, H.; Kanno, M.; Kato, H.; Kobayashi, K.; Kawanishi, A.; Azuma, T.; Muramatsu, M.; Nagahara, S.; Kitano, T.; Toshima, T. *Proc. SPIE* **2012**, *8323*, 83230Y-1−7.
(6) Yi, H.; Bao, X.-Y.; Zhang, J.; Bencher, C.; Chang, L.-W.; Chen, X.; Tiberio, R.; Conway, J.; Dai, H.; Chen, Y.; Mitra, S.; Wong, H.-S. P. *Adv. Mater.* **2012**, *24*, 3107−3114.
(7) Ruiz, R.; Dobisz, E.; Albrecht, T. R. *ACS Nano* **2011**, *5*, 79−84.
(8) Hinsberg, W.; Cheng, J.; Kim, H.-C.; Sanders, D. P. *Proc. SPIE* **2010**, *7637*, 76370G-1−11.
(9) Detcheverry, F. A.; Nealey, P. F.; de Pablo, J. J. *Macromolecules* **2010**, *43*, 6495−6504.
(10) Bita, I.; Yang, J. K. W.; Jung, Y. S.; Ross, C. A.; Thomas, E. L.; Berggren, K. K. *Science* **2008**, *321*, 939−943.
(11) Ruiz, R.; Kang, H.; Detcheverry, F. A.; Dobisz, E.; Kercher, D. S.; Albrecht, T. R.; de Pablo, J. J.; Nealey, P. F. *Science* **2008**, *321*, 936−939.
(12) Yu, B.; Sun, P.; Chen, T.; Jin, Q.; Ding, D.; Li, B.; Shi, A.-C. *J. Chem. Phys.* **2007**, *126*, 204903−1−5.
(13) Cheng, J. Y.; Ross, C. A.; Smith, H. I.; Thomas, E. L. *Adv. Mater.* **2006**, *18*, 2505−2521.
(14) Yu, B.; Sun, P.; Chen, T.; Jin, Q.; Ding, D.; Li, B.; Shi, A.-C. *Phys. Rev. Lett.* **2006**, *96*, 138306−1−4.
(15) Segalman, R. A. *Mater. Sci. Eng., R* **2005**, *48*, 191−226.
(16) Kim, S. O.; Solak, H. H.; Stoykovich, M. P.; Ferrier, N. J.; de Pablo, J. J.; Nealey, P. F. *Nature* **2003**, *424*, 411−414.
(17) Ginzburg, V. V.; Weinhold, J. D.; Trefonas, P. T. *J. Polym. Sci., Part B: Polym. Phys.* **2013**, DOI: 10.1002/polb.23365.
(18) Reilly, M.; Ginzburg, V. V.; Smith, M. D. *Proc. SPIE* **2013**, *8682*, 86820G-1−9.
(19) Yi, H.; Latypov, A.; Wong, H.-S. P. *Proc. SPIE* **2013**, *8680*, 86801L-1−7.
(20) Yi, H.; Bao, X.-Y.; Tiberio, R.; Wong, H.-S. P. *Proc. SPIE* **2013**, *8680*, 868010−1−9.
(21) Laachi, N.; Delaney, K. T.; Kim, B.; Hur, S.-M.; Bristol, R.; Shykind, D.; Weinheimer, C. J.; Fredrickson, G. H. *Proc. SPIE* **2013**, *8680*, 868014−1−9.
(22) Chen, P.; Liang, H.; Xia, R.; Qian, J.; Feng, X. *Macromolecules* **2013**, *46*, 922−926.
(23) Xie, N.; Li, W.; Qiu, F.; Shi, A.-C. *Soft Matter* **2013**, *9*, 536−542.
(24) Takahashi, H.; Laachi, N.; Hur, S.-M.; Wienheimer, C. J.; Shykind, D.; Fredrickson, G. H. *Proc. SPIE* **2012**, *8323*, 83231N-1−6.
(25) Mishra, V.; Fredrickson, G. H.; Kramer, E. J. *ACS Nano* **2012**, *6*, 2629−2641.
(26) Kriksin, Y. A.; Neratova, I. V.; Khalatur, P. G.; Khokhlov, A. R. *Chem. Phys. Lett.* **2010**, *492*, 103−108.
(27) Hur, S.-M.; Garcia-Cervera, C. J.; Kramer, E. J.; Fredrickson, G. H. *Macromolecules* **2009**, *42*, 5861−5872.
(28) Tang, Q.; Ma, Y. *Soft Matter* **2010**, *6*, 4460−4465.
(29) Chang, J.-B.; Son, J. G.; Hannon, A. F.; Alexander-Katz, A.; Ross, C. A.; Berggren, K. K. *ACS Nano* **2012**, *6*, 2071−2077.
(30) Tavakkoli K. G., A.; Gotrik, K. W.; Hannon, A. F.; Alexander-Katz, A.; Ross, C. A.; Berggren, K. K. *Science* **2012**, *336*, 1294−1298.
(31) Tavakkoli K. G., A.; Hannon, A. F.; Gotrik, K. W.; Alexander-Katz, A.; Ross, C. A.; Berggren, K. K. *Adv. Mater.* **2012**, *24*, 4249−4254.
(32) Yang, J. K. W.; Jung, Y. S.; Chang, J.-B.; Mickiewicz, R. A.; Alexander-Katz, A.; Ross, C. A.; Berggren, K. K. *Nat. Nanotechnol.* **2010**, *5*, 256−260.
(33) Kim, S. O.; Kim, B. H.; Meng, D.; Shin, D. O.; Koo, C. M.; Solak, H. H.; Wang, Q. *Adv. Mater.* **2007**, *19*, 3271−3275.
(34) Stoykovich, M. P.; Kang, H.; Daoulas, K. C.; Liu, G.; Liu, C.-C.; de Pablo, J. J.; Müller, M.; Nealey, P. F. *ACS Nano* **2007**, *1*, 168−175.
(35) Stoykovich, M. P.; Müller, M.; Kim, S. O.; Solak, H. H.; Edwards, E. W.; de Pablo, J. J.; Nealey, P. F. *Science* **2005**, *308*, 1442−1446.
(36) Hannon, A. F.; Gotrik, K. W.; Ross, C. A.; Alexander-Katz, A. *ACS Macro Lett.* **2013**, *2*, 251−255.
(37) Qin, J.; Khaira, G. S.; Su, Y.; Garner, G. P.; Miskin, M.; Jaeger, H. M.; de Pablo, J. J. *Soft Matter* **2013**, *9*, 11467−11472.

(38) Chang, J.-B.; Choi H. K.; Hannon, A. F.; Alexander-Katz, A.; Ross, C. A.; Berggren, K. K. Unpublished work.

(39) Cohn, H.; Kumar, A. *Proc. Natl. Acad. Sci. U.S.A.* **2009**, *106*, 9570−9575.

(40) Torquato, S. *Soft Matter* **2009**, *5*, 1157−1173.

(41) Mickiewicz, R. A.; Yang, J. K. W.; Hannon, A. F.; Jung, Y. S.; Alexander-Katz, A.; Berggren, K. K.; Ross, C. A. *Macromolecules* **2010**, *43*, 8290−8295.

(42) Fredrickson, G. H.; Ganesan, V.; Drolet, F. *Macromolecules* **2002**, *35*, 16−39.

(43) Fredrickson, G. H. *The Equilibrium Theory of Inhomogeneous Polymers*; Oxford University Press: Oxford, England, 2006.

(44) Gotrik, K. W.; Hannon, A. F.; Son, J. G.; Keller, B.; Alexander-Katz, A.; Ross, C. A. *ACS Nano* **2012**, *6*, 8052−8059.